Editors' Suggestion

X-Ray Free-Electron Laser Observation of Giant and Anisotropic Magnetostriction in β-O_2 at 110 Tesla

Akihiko Ikeda,[1,*,†] Yuya Kubota,[2,*,‡] Yuto Ishii,[3] Xuguang Zhou,[3] Shiyue Peng,[3] Hiroaki Hayashi,[3] Yasuhiro H. Matsuda,[3] Kosuke Noda,[1] Tomoya Tanaka,[1] Kotomi Shimbori,[1] Kenta Seki,[1] Hideaki Kobayashi,[1] Dilip Bhoi,[1] Masaki Gen,[3,4] Kamini Gautam,[4] Mitsuru Akaki,[5] Shiro Kawachi,[6] Shusuke Kasamatsu,[7] Toshihiro Nomura,[8] Yuichi Inubushi,[2,9] and Makina Yabashi[2,9]

[1]*Department of Engineering Science, University of Electro-Communications, Chofu, Tokyo 182-8585, Japan*
[2]*RIKEN SPring-8 Center, Sayo, Hyogo 679-5148, Japan*
[3]*Institute for Solid State Physics, University of Tokyo, Kashiwa, Chiba 277-8581, Japan*
[4]*RIKEN Center for Emergent Matter Science (CEMS), Wako 351-0198, Japan*
[5]*Institute for Material Research, Tohoku University, Sendai, Miyagi 980-8577, Japan*
[6]*Graduate School of Science, University of Hyogo, Koto, Hyogo 678-1297, Japan*
[7]*Faculty of Science, Yamagata University, Kojirakawa, Yamagata 990-8560, Japan*
[8]*Department of Physics, Faculty of Science, Shizuoka University, Shizuoka 422-8529, Japan*
[9]*Japan Synchrotron Radiation Research Institute (JASRI), Sayo, Hyogo 679-5198, Japan*

(Received 20 May 2025; revised 18 July 2025; accepted 19 September 2025; published 28 October 2025)

In strong magnetic fields beyond 100 T, the significant Zeeman energy competes with the lattice interactions, where a considerable magnetostriction is expected. However, the microscopic observation of the magnetostriction above 100 T has been hindered due to the short pulse duration of microseconds and the coil's destruction. Here, we report the observation of the giant and anisotropic magnetostriction of ~1% at 110 T in the spin-controlled crystal β-O_2 by combining the single-shot diffraction of an x-ray free-electron laser (XFEL) and the newly developed portable 100 T generator (PINK-02). The soft and anisotropic response of β-O_2 should originate in the competing van der Waals force and exchange interaction and also the frustration of spin and lattice on the triangular network. The XFEL experiment above 100 T using PINK-02 enables microscopic investigations on materials' properties at high magnetic fields, providing insights into how spins contribute to the stability of crystal structures.

DOI: 10.1103/r7br-qnrn

Magnetic fields are fertile ground for novel findings in diverse scientific disciplines, ranging from condensed matter physics and planetary science to biological science. The primary objective of applied magnetic fields on materials of a few to a few tens of Tesla are to see and change the electronic and magnetic states [1,2], which is constrained by the limited scale of Zeeman energy [3]. On the other hand, magnetic fields beyond ~100–1000 T are the frontier where they are expected to break the crystal state of materials. Zeeman energy at 1000 T amounts to 1340 K, which competes the crystal lattice's energy. Even with a magnetostriction of $\Delta L/L = 10^{-6}$ at 1 T, the extrapolation with the relation $\Delta L/L \propto B^2$ gives a significant magnetostriction of 1% and 100% at 100 and 1000 T, respectively, making us believe that some drastic change in the relation between spin and lattice happens above 100 T. Meanwhile, the magnetic field can also be a valuable tool for modifying the crystal in a manner distinct from other stimuli, such as pressure, strain, chemical substitution, and photoirradiation.

Solid O_2, a spin-controlled crystal, is the representative candidate for a magnetic-field-induced lattice change where the strong spin-lattice coupling is in play [4,5]. O_2 is a molecular magnet with $S = 1$ with molecular orbital state $^3\sum_g^-$ as depicted in Fig. 1(a). Upon cooling, it condenses into a liquid and then three distinct solids, γ-O_2, β-O_2, and α-O_2. The variety of the solid phases is the manifestation of the competing interactions in solid O_2 such as van der Waals interaction, the interaction between the electric quadrupole moments (these two factors breed the exotic phase diagram of solid N_2 [6]), and the antiferromagnetic exchange interactions between the molecular spins, as schematically shown in Fig. 1(b). The competing nature in solid O_2 is even more evident in extreme conditions [5]. Under high

*These authors contributed equally to this work.
†Contact author: a-ikeda@uec.ac.jp
‡Contact author: kubota@spring8.or.jp

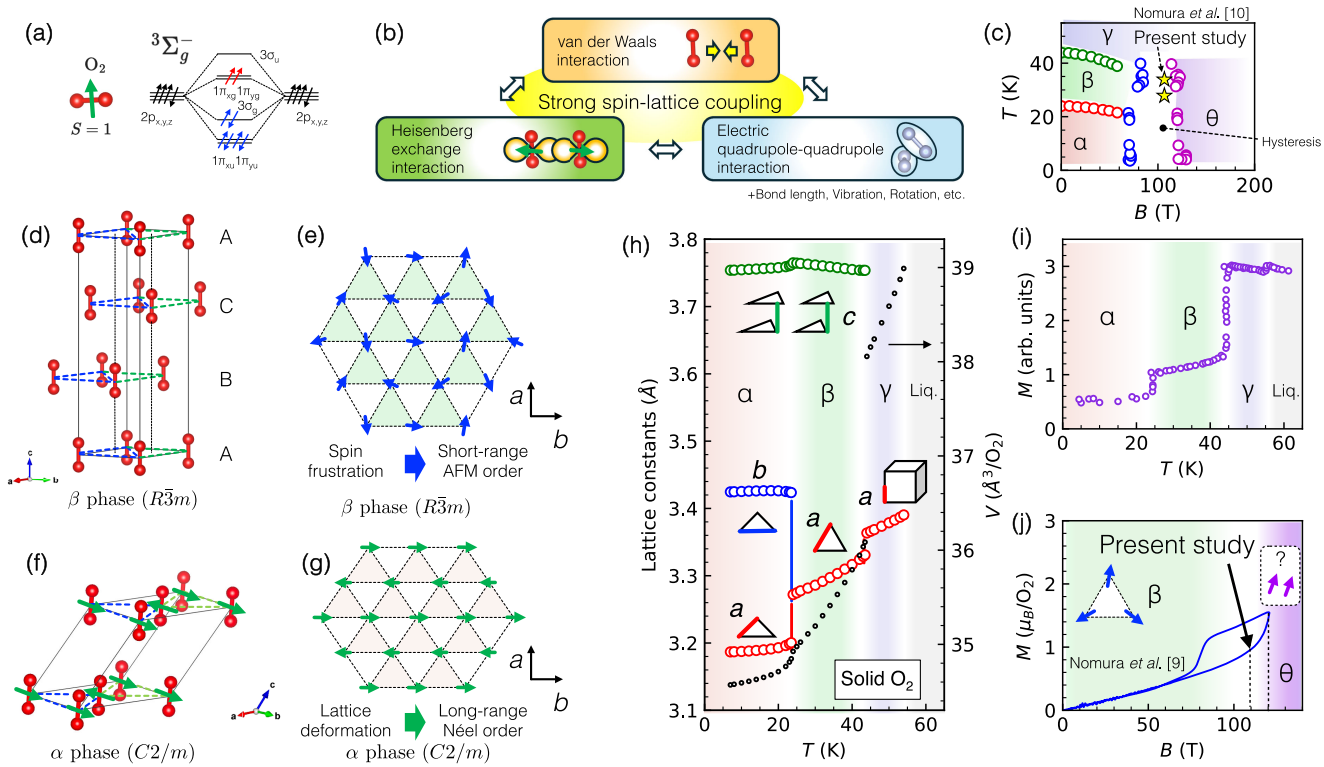

FIG. 1. (a) The molecular orbital of O_2 with $S = 1$. (b) The competing interactions in solid O_2. (c) A phase diagram of solid O_2 on a temperature-magnetic field plane reproduced from Ref. [10]. (d) The crystal structure of β-O_2 whose space group is $R\bar{3}m$. Layers of a triangular lattice are stacked vertically in the *ABC-ABC* manner. (e) The schematic of spin configuration on the triangular lattice of β-O_2. Because of an intense frustration from the lattice symmetry, the spin shows a short-range order with a 140° structure [13]. (f) The crystal structure of α-O_2 whose space group is $C2/m$. It is a deformed structure of β-O_2. In the layer, the triangle lattice is deformed so that the spin frustration is relaxed. (g) The schematics for the arrangement of the Néel order of spins on the deformed triangular lattice in α-O_2, which results in the nonequivalent exchange constant in a and b direction. (h) The temperature dependence of lattice parameters and volume in solid O_2. The data are extracted from Ref. [4]. (i) The temperature dependence of magnetization of solid O_2. The data are extracted from Ref. [14]. (j) The magnetization of solid O_2 at 32 K up to 124 T. The data are adopted from Ref. [9]. Magnetic-field-induced phase transition from β-O_2 to θ-O_2 occurs above 120 T. In the present Letter, we generated up to 110 T, where we obtained XRD of the strained β-O_2 by magnetostriction.

pressure, three more phases show up, where the metallic phase emerges beyond 100 GPa, which becomes superconducting below 0.6 K [7]. Above an ultrahigh magnetic field of 120 T, the ferromagnetic solid O_2, θ-O_2, was discovered a decade ago, as shown in Figs. 1(c) and 1(j) [8–12].

We work on β-O_2, which exhibits softness and fluctuations in lattice and magnetism. The crystal structure of β-O_2 is represented by the triangular lattice in the a-b plane, which is stacked in the c axis. The molecular axis aligns perpendicular to the a-b plane to enhance the exchange interaction between molecular spins by maximizing the overlap of the π orbitals, as schematically shown in Fig. 1(d). The spin interaction in β-O_2 is represented by the Heisenberg model with $S = 1$ on the triangular lattice, which faces the geometrical frustration, resulting in the suppression of the long-range order and realization of the short-range antiferromagnetic order of 140° structure [13], as shown in Fig. 1(e). Below 24 K, the lattice exhibits a first-order structural transition to α-O_2 with monoclinic structure as shown in Fig. 1(f), where the triangle lattice becomes significantly deformed in the a-b plane. This relaxes the geometrical frustration of the spin system, resulting in the long-range Néel order as shown in Fig. 1(g). The deformation is evident in the lattice constant in Fig. 1(h), showing the splitting of the length of the sides of the triangle by 7% upon entering the α phase. Meanwhile, the magnetization shows a sudden decrease upon entering the α phase from the β phase, as shown in Fig. 1(i). Surprisingly, the lattice parameter change of the a-b plane in β-O_2 amounts to 2% in the limited temperature range from 24 to 44 K. In contrast, comparably small changes $< 0.5\%$ are observed in the c axis in β-O_2 in the same temperature range. This is due to the soft triangular lattice, which is realized by the geometrical frustration of the spin system on the triangular lattice unique to the a-b plane of β-O_2 with the strong spin-lattice coupling [15].

When ultrahigh magnetic fields beyond 100 T are applied to that spin-lattice coupled system, we expect drastic changes in the crystal parameters. Indeed, the ferromagnetic θ-O_2 is

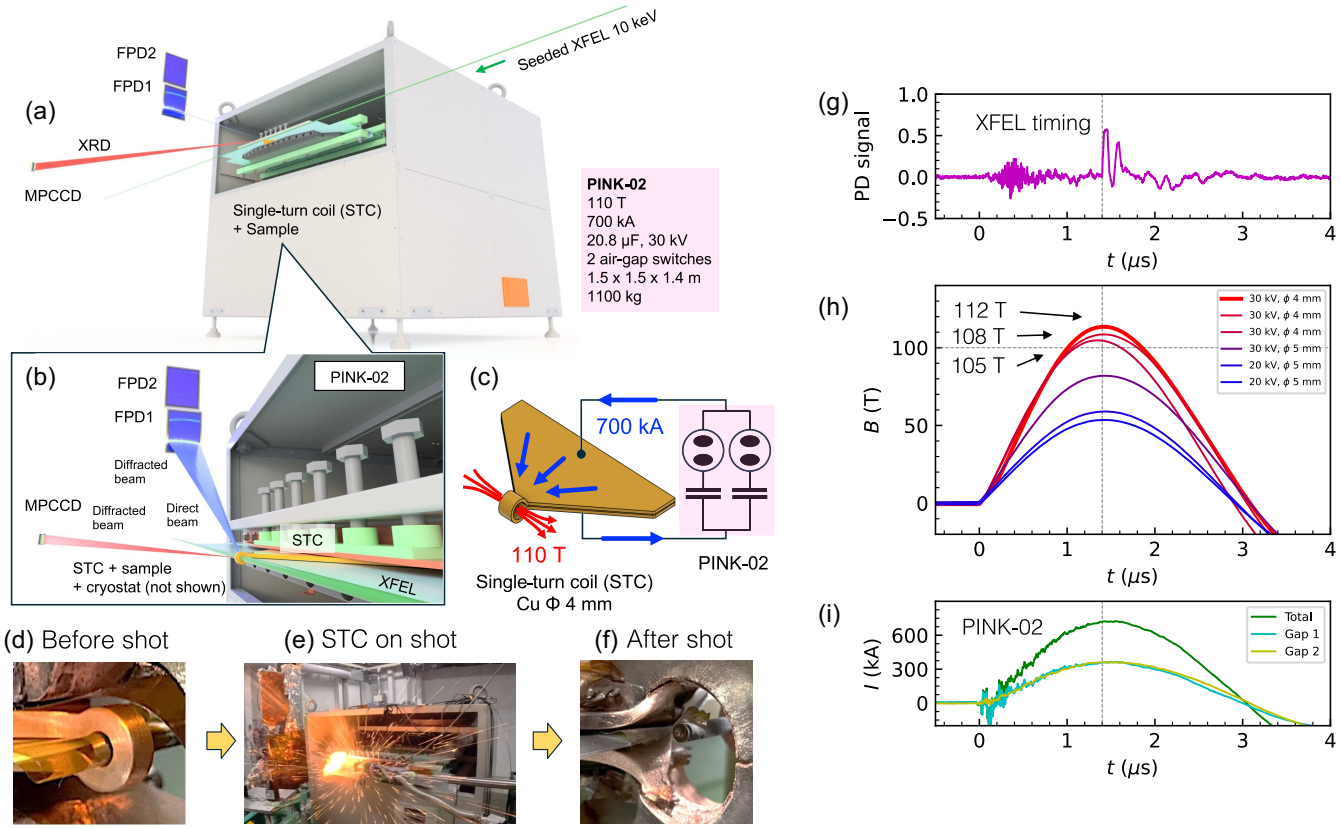

FIG. 2. (a) A schematic view of PINK-02 and the arrangement for the XRD in combination with the XFEL installed in SACLA. (b) A magnification at the single-turn coil (STC) and x-ray beam incident on the sample, with diffracted beams propagating to the two-dimensional (2D) x-ray detectors. (c) A schematic drawing of the electric circuit of PINK-02 and a single-turn coil. (d) A photo of a single-turn coil of $\phi 4$ mm before the shot. (e) A photo of the single-turn coil during the magnetic field generation. (f) A photo of a single-turn coil after the shot. (g) X-ray photodiode (PD) signal intensity as a function of time. (h) Representative waveforms of pulsed magnetic field generated using PINK-02 with single-turn coils of $\phi 4$ and 5 mm diameter and charging voltages of 20 and 30 kV. (i) Representative waveforms of the current injected into the single-turn coil. There are two switches connected in parallel.

discovered above 120 T as shown in Fig. 1(j) [8–12], where the determination of crystal structure change has remained elusive. For this purpose, we have realized a method for the macroscopic measurement of $\Delta L/L$ beyond 100 T employing the fiber Bragg grating (FBG) method [16], which has been applied to various systems [17–22] up to 600 T, generated using the single-turn coil method and the electromagnetic flux compression method [23]. To gain further insights into the spin-lattice coupling beyond 100 T, one needs the microscopic probes, such as x-ray diffraction (XRD), in addition to the FBG dilatometry. However, x-ray diffractometry at 100 T is experimentally challenging because experimentally obtaining 100 T necessitates destructive pulse magnets [24]. To overcome the difficulty, we reported an XRD study with a generation of 77 T pulsed magnetic field by implementing the first portable intense kyokugenjiba, i.e., "extreme magnetic field" (PINK-01) in combination with the single-shot powder diffraction of an x-ray free-electron laser (XFEL) from a solid sample [25,26]. Although the microsecond pulse of 77 T generated using destructive magnets was shown to be compatible with the XFEL pulses, the field strength of PINK-01 is not sufficient for the exploration beyond 100 T.

Here, we present the portable generation of 110 T using the newly devised PINK-02, which goes with the single-shot XRD for β-O_2. The setup is depicted in Figs. 2(a) and 2(b). PINK-02 employs two capacitors of 20.8 μF in total rated at 30 kV, equipped with discharge air-gap switches as schematically depicted in Fig. 2(c), which weighs 1100 kg. The capacitance and rated current of PINK-02 are twice those of PINK-01. By injecting the current into the single-turn coil, one can obtain the ultrahigh magnetic field, where the single-turn coil explodes at each shot, as shown in Figs. 2(d)–2(f) and the End Matter. The average magnetic field obtained was 110 ± 5 T with the inner diameter of 4 mm, as schematically shown in Fig. 2(h), where the maximum current and voltage are about 700 kA and 30 kV, respectively, as shown in Fig. 2(i). The pulse duration of the magnetic field was 3 μs, whose maximum timing is well synchronized with the XFEL pulse as shown in Fig. 2(g). The experiment was carried out at beamline 3 (BL3) at SPring-8 Angstrom Compact free-electron LAser facility (SACLA) [27]. XFEL pulses at

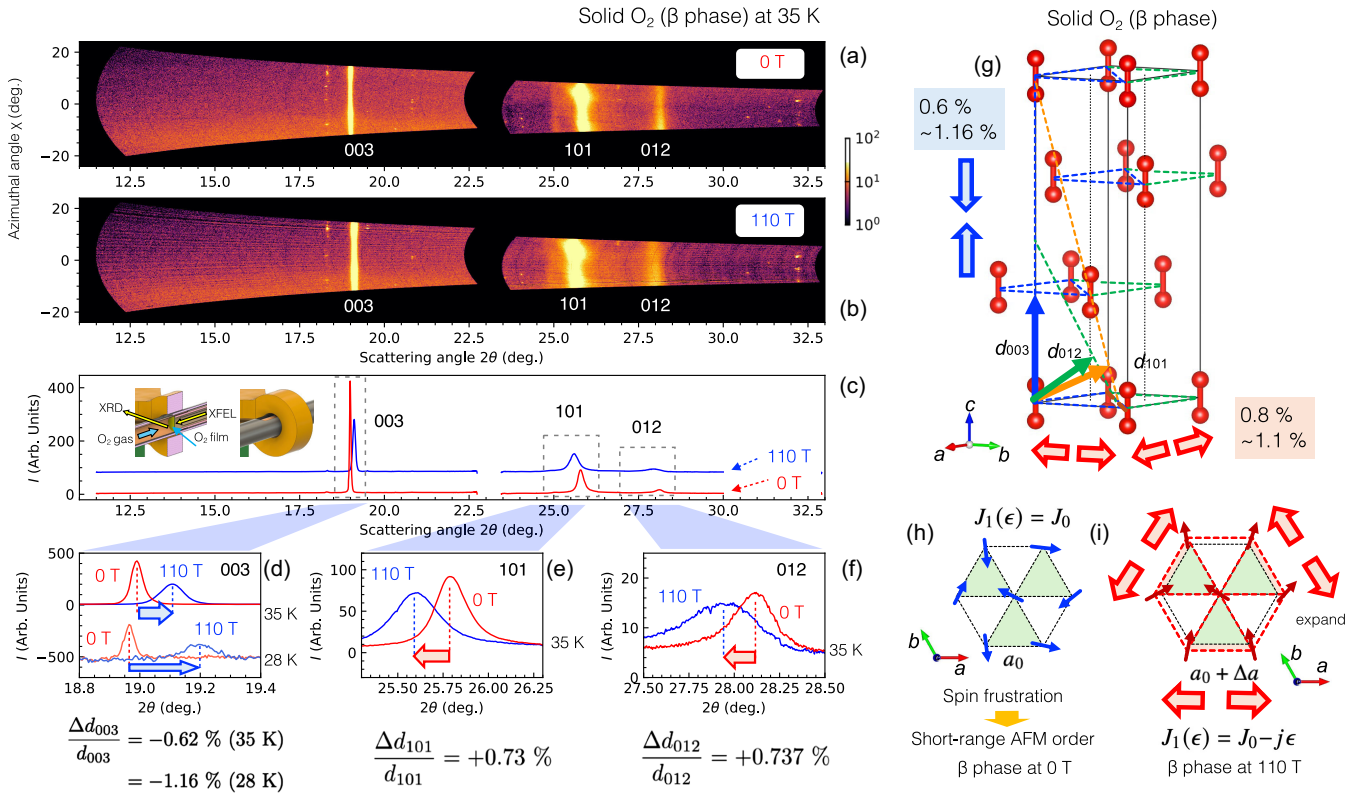

FIG. 3. (a) Powder XRD data from β-O_2 recorded using 2D x-ray detectors at 0 T and (b) at 110 T. (c) Integrated powder XRD data from β-O_2 at 0 and 110 T. Inset: the schematic drawing of the experimental setup at the sample position. (d) The magnified powder XRD data at the 003 reflection of β-O_2 at 35 and 28 K, showing -0.62 and -1.16% shrinkage of the interplane separation at 110 T, respectively. (e) The magnified data of powder XRD at the 101 reflection of β-O_2 at 35 K, showing $+0.73\%$ elongation of the interplane separation at 110 T. (f) The magnified data of powder XRD at the 012 reflection of β-O_2 at 35 K, showing $+0.737\%$ elongation of the interplane separation at 110 T. (g) The schematic drawing of the crystal structure of β-O_2 with the indication of the shrinkage in the c axis and elongation in the a-b plane. The diffraction planes are also depicted. (h) The schematic drawing of the crystal structure and spin configuration in β-O_2 at 0 T, where the O_2 molecules form the triangular lattice with the short-range order due to the antiferromagnetic coupling and geometrical frustration. (i) The schematic drawing of the crystal structure and spin configuration in β-O_2 at 110 T, where the spins are more aligned to the external magnetic field, losing the antiferromagnetic short-range order. This results in the expansion of the lattice parameter in the a-b plane to relax the antiferromagnetic exchange coupling between spins.

10 keV with self-seeding [28] with a dispersion of 1–3 eV with ~360 μJ/pulse are delivered to the powder sample.

The results of the powder XRD of β-O_2 obtained at 0 and 110 T are displayed in the full image of the x-ray detector in Figs. 3(a) and 3(b), respectively. They show three XRD peaks from solid O_2, 003, 101, 012, by which the solid O_2 is attributed to be in β-O_2. By comparing the data in Figs. 3(a) and 3(b), one can tell that the peak positions are shifted in the data at 110 T. The shift is qualitatively shown in the plots in Figs. 3(c)–3(f), where the signs of the shifts are dependent on the diffraction indexes. In the present experimental geometry, the observed lattice strain is transverse primarily rather than longitudinal magnetostriction. Although we obtained only two datasets in the present Letter, the reliability of our measurement is ensured by several other samples, including $CuGaCr_4S_8$ [29].

The anisotropic magnetostriction is evidenced by observing the positive shift of the 003 diffraction angle and the negative shift of the 101 and 012 diffraction angles, respectively, at 110 T. In Fig. 3(d), the 003 diffraction peak at 28 K is shown along with that at 35 K, where the scattering angles 2θ show shifts from 18.99° to 19.11° and from 18.965° to 19.19°, respectively. With the definition $\Delta d_{hkl}/d_{hkl} \equiv (d_{hkl}^{110\,\mathrm{T}}/d_{hkl}^{0\,\mathrm{T}}) - 1 = (\sin\theta_{hkl}^{0\,\mathrm{T}}/\sin\theta_{hkl}^{110\,\mathrm{T}}) - 1$ [30], the values of $\Delta d_{003}/d_{003} = -0.62\%$ and -1.16% are deduced, respectively, which readily correspond to the shrinkage of the c axis ($\Delta c/c < 0$) as shown in Fig. 3(g). These are twice the value of the thermally induced change of the c axis in the β phase as shown in Fig. 1(i), which is only 0.5%.

In Figs. 3(e) and 3(f), for the 101 and 012 diffraction peaks, 2θ show shifts from 25.79° to 25.6° and from 28.12° to 27.91°, respectively. The deduced values are $\Delta d_{101}/d_{101} = +0.73\%$ and $\Delta d_{012}/d_{012} = +0.737\%$, respectively. With the pairs of the values $\Delta d_{hkl}/d_{hkl}$ ($hkl = 003$ and 101, or 003 and 012), one can deduce the values of $\Delta a/a = 0.8$ or 1.1%,

respectively. The reason for the discrepancy in the values is unclear. With an averaged value $\Delta a/a = 0.95\%$ and $\Delta c/c = -0.62\%$ at 110 T and 35 K, one can deduce the following the values: the volume expansion $\Delta V/V \equiv \Delta c/c + \Delta a/a \times 2 = 1.28\%$ and the distortion value $\Delta D/D \equiv \Delta c/c - \Delta a/a = -1.57\%$. Note that $\Delta D/D = 0$ if the lattice change is isotropic (i.e., $\Delta a/a = \Delta c/c$). The anisotropic and significant magnetostriction is indicated by the obtained values of $\Delta a/a = 0.95\%$, $\Delta c/c = -0.62\%$, $\Delta V/V = 1.28\%$, and $\Delta D/D = -1.57\%$ in the β phase of solid O_2 at 110 T and 35 K. An even more significant value of $\Delta c/c = -1.16\%$ at 110 T and 28 K is noteworthy.

We discuss the origin of the observed anisotropic magnetostriction. β-O_2 is regarded as a two-dimensional spin system, where the exchange interaction is strong within the a-b plane and subtle between the planes [4]. To discuss this in detail, we consider a two-dimensional Heisenberg model with exchange striction, as follows [31], $\mathcal{H} = \sum_{\langle i,j \rangle} J_1(\mathbf{R}_{i,j})\hat{\mathbf{S}}_i \cdot \hat{\mathbf{S}}_j + k\epsilon^2/2 - g\mu_B \sum_i \hat{\mathbf{S}}_i \cdot \mathbf{B}$, where $J_1(\mathbf{R}_{i,j})$, $\langle i, j \rangle$, $\hat{\mathbf{S}}_i$, k, ϵ, g, μ_B, and $\mathbf{B}$ are exchange constant dependent on intermolecular arrangement $\mathbf{R}_{i,j}$, pairs of the nearest-neighbor sites, spin operator, the elastic constant, and the lattice strain, g factor, Bohr magneton, magnetic field. The first, second, and third terms of the Hamiltonian describe the antiferromagnetic exchange coupling between spins on the nearest neighboring sites of the triangle lattice, the elastic energy of the lattice in the a-b plane, and the Zeeman energy for individual spins, respectively. For simplicity, we consider that $J_1(\mathbf{R}_{i,j})$ depends on ϵ. We obtain $J_1(\epsilon) = J_0 - j\epsilon$, where J_0 and j are the exchange constant without strain and the coefficient for the strain-dependent change of the exchange constant. The Hamiltonian explains the lattice expansion in the a-b plane. First, the magnetization gradually increases up to 0.9 μ_B/O_2 [9] at 110 T, where the Heisenberg term of the Hamiltonian increases the total energy. The system attempts to compensate for the increased energy by minimizing the exchange constant $J_1(\epsilon)$, which is achieved by increasing the intermolecular distance in the a-b plane with a decrease of the energy of $j\epsilon\langle \hat{\mathbf{S}}_i \cdot \hat{\mathbf{S}}_j \rangle$. ϵ increases until the Heisenberg energy is equilibrated with the rise of the elastic energy $k\epsilon^2/2$.

To gain qualitative insights into the balance of the elastic energy and the exchange energy, we refer to the spin-dependent intermolecular potential calculated for the dimer $(O_2)_2$ in the parallel (H) geometry [32] and the spin-spin exchange constant J_1 estimated in a high-pressure experiment [33], which shows a qualitative agreement with our discussion. Figures 4(a) and 4(b) show the intermolecular potential as a function of the intermolecular distance R with a variation of $S_{(O_2)_2} = 0$, 1, and 2 [32], which is fitted to the Morse potential [34]. As shown in Fig. 4(b), with increasing R by 1% from the equilibrium position, the increase of the elastic energy ($k\epsilon^2/2$) is ~1 K/bond, which amounts to

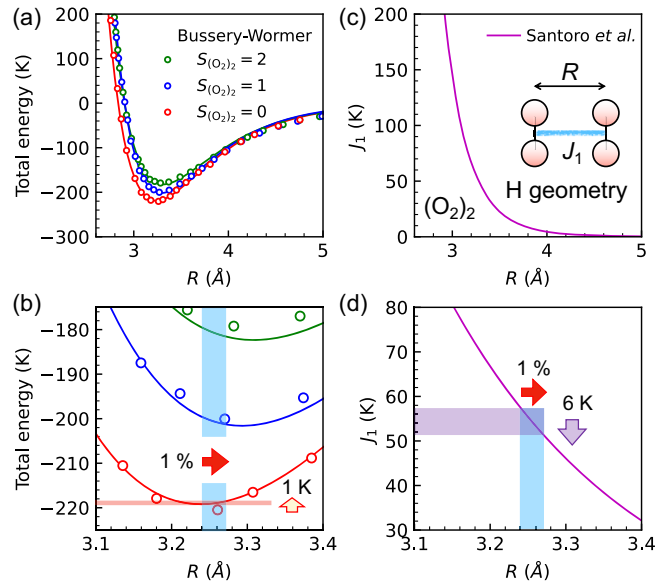

FIG. 4. (a) Intermolecular potential of the dimer $(O_2)_2$ calculated as a function of the intermolecular distance R in H geometry with a variation of the total spin $S_{(O_2)_2} = 0$, 1, and 2 [32]. (b) A magnification of (a). (c) Exchange constant J_1 of between molecular spins as a function of R deduced from the high-pressure experiment [33]. (d) A magnification of (c).

+3 K/O_2. Further, the dependence of J_1 on the intermolecular distance of O_2 is estimated in a high-pressure study of solid O_2 [33], as shown in Figs. 4(c) and 4(d). With increasing R by 1%, the decrease of J_1 ($= j\epsilon$) is ~ -6 K/bond. With the magnetization value at 110 T of $g\mu_B\langle S^z \rangle = 0.9\ \mu_B$ [9] and assuming $j\epsilon\langle \hat{\mathbf{S}}_i \cdot \hat{\mathbf{S}}_j \rangle \simeq j\epsilon\langle \hat{S}_i^z \rangle \langle \hat{S}_j^z \rangle$, the reduction of the exchange energy amounts to ~ -3.6 K/O_2. One finds that it is a comparable value for the aforementioned increase of the elastic energy.

The qualitative argument above with the dimer $(O_2)_2$ is further strengthened by our first-principles calculation of the exchange constants in the solid β phase with the structure of 0 T and the deformed unit cell at 110 T obtained in the present Letter. Here, we denote the nearest-neighbor exchange interaction in the a-b plane direction and in the interlayer (c) direction as J_1 and J_2, respectively. The calculation employs the van der Waals (vdW) density functional theory and the tight-binding model calculation. The calculated result of $J_1(0\ \text{T})$ and $J_1(110\ \text{T})$ are 47.35 and 41.8 K/bond, where $\Delta J_1 = -5.55$ K is an 11.8% reduction of the antiferromagnetic interaction, being in good agreement with the reported results on the dimer $(O_2)_2$ as shown in Fig. 4(d) and the exchange striction mechanism driving the expansion in the a-b plane. The calculated result of $J_2(0\ \text{T})$ and $J_2(110\ \text{T})$ are 6.5 and 7.4 K/bond, where $\Delta J_2 = +0.9$ K is an 14.3% increase of the antiferromagnetic interaction. ΔJ_2 is less significant than ΔJ_1 and the sign counters to the observed lattice change. This indicates that the shrinkage in the c axis at

110 T is not driven by the exchange striction mechanism with ΔJ_2, which accords with the previous notion that the interlayer coupling of spins is negligible due to the small hybridization of the π orbitals [35]. Another possible mechanism for the shrinkage in the c axis is the conservation effect of the lattice volume expansion with the expanding a-b plane, which is not conclusive.

In conclusion, we obtained powder XRD data of β-O_2 at 110 T by establishing the novel portable 100 T technique PINK-02 compatible with XFEL. An anisotropic lattice deformation of up to 1% was observed, which arises from the two dimensionality of the spin system and the competition between exchange and van der Waals interactions. Our method opens the way to exploring spin-lattice coupling phenomena above 100 T. The clarification of the crystal structure of θ-O_2 is, without a doubt, the most crucial goal of our Letter to follow.

The obtained image [Figs. 3(a)–3(f)] is analyzed using a Python package pyFAI [36]. The crystal structures are rendered using the 3D visualization tool VESTA [37].

Acknowledgments—Fruitful discussion with J. Nasu is acknowledged. The experiment was conducted with the approval of JASRI (Proposals No. 2024A8010 and No. 2024B8046). The authors would like to acknowledge the support from the technical staff of the SACLA facility. PINK-02 is established with the support of the SACLA/SPring-8 Basic Development Program (2021–2024). This work is supported by the JST FOREST (Programs No. JPMJFR222W and No. JPMJFR2037), JSPS Grant-in-Aid for Scientific Research on Innovative Areas (A) (1000 T Science) No. 23H04859, No. 23H04860, No. 23H04861, No. 23H04865, and No. 24H01633, Grant-in-Aid for Scientific Research (B) No. 23H01121, Grant-in-Aid for Scientific Research No. 24K21043, and MEXT LEADER Program No. JPMXS0320210021.

Data availability—The data that support the findings of this article are openly available [38].

[1] S. Gerber *et al.*, Three-dimensional charge density wave order in $YBa_2Cu_3O_{6.67}$ at high magnetic fields, Science **350**, 949 (2015).

[2] S. Ran, I.-L. Liu, Y. S. Eo, D. J. Campbell, P. M. Neves, W. T. Fuhrman, S. R. Saha, C. Eckberg, H. Kim, D. Graf, F. Balakirev, J. Singleton, J. Paglione, and N. P. Butch, Extreme magnetic field-boosted superconductivity, Nat. Phys. **15**, 1250 (2019).

[3] Zeeman energy mounts to over 1.34 K for a free-electron spin at 1 T with the relation $E_{\mathrm{Zeeman}} = g\mu_{\mathrm{B}} S_z B_z$, where g, μ_{B}, S_z, and B_z are g factors, Bohr magneton, spin, and external magnetic field, respectively.

[4] Y. A. Freiman and H. J. Jodl, Solid oxygen, Phys. Rep. **401**, 1 (2004).

[5] Y. A. Freiman, H. J. Jodl, and Y. Crespo, Solid oxygen revisited, Phys. Rep. **743**, 1 (2018).

[6] M. Kirsz, C. G. Pruteanu, P. I. C. Cooke, and G. J. Ackland, Understanding solid nitrogen through molecular dynamics simulations with a machine-learning potential, Phys. Rev. B **110**, 184107 (2024).

[7] K. Shimizu, K. Suhara, M. Ikumo, M. I. Eremets, and K. Amaya, Superconductivity in oxygen, Nature (London) **393**, 767 (1998).

[8] T. Nomura, Y. H. Matsuda, S. Takeyama, A. Matsuo, K. Kindo, J. L. Her, and T. C. Kobayashi, Novel phase of solid oxygen induced by ultrahigh magnetic fields, Phys. Rev. Lett. **112**, 247201 (2014).

[9] T. Nomura, Y. H. Matsuda, S. Takeyama, A. Matsuo, K. Kindo, and T. C. Kobayashi, Phase boundary of θ phase of solid oxygen in ultrahigh magnetic fields, Phys. Rev. B **92**, 064109 (2015).

[10] T. Nomura, Y. H. Matsuda, and T. C. Kobayashi, H-T phase diagram of solid oxygen, Phys. Rev. B **96**, 054439 (2017).

[11] T. Nomura, Y. Kohama, Y. H. Matsuda, K. Kindo, and T. C. Kobayashi, α-β and β-γ phase boundaries of solid oxygen observed by adiabatic magnetocaloric effect, Phys. Rev. B **95**, 104420 (2017).

[12] T. Nomura, Y. H. Matsuda, and T. C. Kobayashi, Solid and liquid oxygen under ultrahigh magnetic fields, Oxygen **2**, 152 (2022).

[13] F. Dunstetter, V. P. Plakhti, and J. Schweizer, The magnetic structure of β oxygen: A neutron polarisation analysis study, J. Magn. Magn. Mater. **72**, 258 (1988).

[14] R. J. Meier, C. J. Schinkel, and A. d. Visser, Magnetisation of condensed oxygen under high pressures and in strong magnetic fields, J. Phys. C **15**, 1015 (1982).

[15] A. S. Baryl'nik and A. I. Prokhvatilov, Spontaneous magnetostriction effects in α- and β-phases of oxygen, Low Temp. Phys. **20**, 716 (1994).

[16] A. Ikeda, T. Nomura, Y. H. Matsuda, S. Tani, Y. Kobayashi, H. Watanabe, and K. Sato, High-speed 100 MHz strain monitor using fiber Bragg grating and optical filter for magnetostriction measurements under ultrahigh magnetic fields, Rev. Sci. Instrum. **88**, 083906 (2017).

[17] A. Ikeda, Y. H. Matsuda, K. Sato, and J. Nasu, A review on magnetic field induced spin crossover in $LaCoO_3$ up to 600 T, J. Phys. Soc. Jpn. **93**, 121005 (2024).

[18] A. Ikeda, Y. H. Matsuda, and K. Sato, Two spin-state crystallizations in $LaCoO_3$, Phys. Rev. Lett. **125**, 177202 (2020).

[19] T. Nomura, A. Ikeda, M. Gen, A. Matsuo, K. Kindo, Y. Kohama, Y. H. Matsuda, S. Zherlitsyn, J. Wosnitza, H. Tsuda, and T. C. Kobayashi, Physical properties of liquid oxygen under ultrahigh magnetic fields, Phys. Rev. B **104**, 224423 (2021).

[20] A. Ikeda, Y. H. Matsuda, K. Sato, Y. Ishii, H. Sawabe, D. Nakamura, S. Takeyama, and J. Nasu, Signature of spin-triplet exciton condensations in $LaCoO_3$ at ultrahigh magnetic fields up to 600 T, Nat. Commun. **14**, 1744 (2023).

[21] T. Nomura, P. Corboz, A. Miyata, S. Zherlitsyn, Y. Ishii, Y. Kohama, Y. H. Matsuda, A. Ikeda, C. Zhong, H. Kageyama, and F. Mila, Unveiling new quantum phases in the Shastry-Sutherland compound $SrCu_2(BO_3)_2$ up to the saturation magnetic field, Nat. Commun. **14**, 3769 (2023).

[22] M. Gen, A. Ikeda, K. Aoyama, H. O. Jeschke, Y. Ishii, H. Ishikawa, T. Yajima, Y. Okamoto, X. Zhou, D. Nakamura,

S. Takeyama, K. Kindo, Y. H. Matsuda, and Y. Kohama, Signatures of a magnetic superstructure phase induced by ultrahigh magnetic fields in a breathing pyrochlore antiferromagnet, Proc. Natl. Acad. Sci. U.S.A. **120**, e2302756120 (2023).

[23] D. Nakamura, A. Ikeda, H. Sawabe, Y. H. Matsuda, and S. Takeyama, Record indoor magnetic field of 1200 T generated by electromagnetic flux-compression, Rev. Sci. Instrum. **89**, 095106 (2018).

[24] F. Herlach, Pulsed magnets, Rep. Prog. Phys. **62**, 859 (1999).

[25] A. Ikeda, Y. H. Matsuda, X. Zhou, S. Peng, Y. Ishii, T. Yajima, Y. Kubota, I. Inoue, Y. Inubushi, K. Tono, and M. Yabashi, Generating 77 T using a portable pulse magnet for single-shot quantum beam experiments, Appl. Phys. Lett. **120**, 142403 (2022).

[26] A. Ikeda, Y. H. Matsuda, X. Zhou, T. Yajima, Y. Kubota, K. Tono, and M. Yabashi, Single shot x-ray diffractometry in SACLA with pulsed magnetic fields up to 16 T, Phys. Rev. Res. **2**, 043175 (2020).

[27] T. Ishikawa *et al.*, A compact x-ray free-electron laser emitting in the sub-ångström region, Nat. Photonics **6**, 540 (2012).

[28] I. Inoue, T. Osaka, T. Hara, T. Tanaka, T. Inagaki, T. Fukui, S. Goto, Y. Inubushi, H. Kimura, R. Kinjo, H. Ohashi, K. Togawa, K. Tono, M. Yamaga, H. Tanaka, T. Ishikawa, and M. Yabashi, Generation of narrow-band x-ray free-electron laser via reflection self-seeding, Nat. Photonics **13**, 319 (2019).

[29] M. Gen, K. Noda, K. Shimbori, T. Tanaka, D. Bhoi, K. Seki, H. Kobayashi, K. Gautam, M. Akaki, Y. Ishii, Y. H. Matsuda, Y. Kubota, Y. Inubushi, M. Yabashi, Y. Kohama, T. Arima, and A. Ikeda, X-ray diffraction study of the magnetization plateau above 40 T in the frustrated helimagnet $CuGaCr_4S_8$, Phys. Rev. B **111**, 214441 (2025).

[30] Deduced from the following relation: $\lambda = 2d_{hkl}^{0\ \mathrm{T}} \sin(\theta_{hkl}^{0\ \mathrm{T}}) = 2d_{hkl}^{110\ \mathrm{T}} \sin(\theta_{hkl}^{110\ \mathrm{T}})$.

[31] A. Ikeda, S. Furukawa, O. Janson, Y. H. Matsuda, S. Takeyama, T. Yajima, Z. Hiroi, and H. Ishikawa, Magnetoelastic couplings in the deformed kagome quantum spin lattice of volborthite, Phys. Rev. B **99**, 140412(R) (2019).

[32] B. Bussery and P. E. S. Wormer, A van der Waals intermolecular potential for $(O_2)_2$, J. Chem. Phys. **99**, 1230 (1993).

[33] M. Santoro, F. A. Gorelli, L. Ulivi, R. Bini, and H. J. Jodl, Antiferromagnetism in the high-pressure phases of solid oxygen: Low-energy electronic transitions, Phys. Rev. B **64**, 064428 (2001).

[34] $M(R) = d\left(1 - \{1 - \exp[-(R - R_0)/a]\}^2\right)$ with d, a, and R_0 being the depth, the inverted width, and the equilibrium position of the potential, respectively.

[35] B. Bussery, S. Y. Umanskii, M. Aubert-Frécon, and O. Bouty, Exchange interaction between two O_2 molecules using the asymptotic method, J. Chem. Phys. **101**, 416 (1994).

[36] J. Kieffer and D. Karkoulis, pyFAI, a versatile library for azimuthal regrouping, J. Phys. Conf. Ser. **425**, 202012 (2013).

[37] K. Momma and F. Izumi, VESTA3 for three-dimensional visualization of crystal, volumetric, and morphology data, J. Appl. Crystallogr. **44**, 1272 (2011).

[38] A. Ikeda, Data: X-ray free-electron laser observation of giant and anisotropic magnetostriction in β-O2 at 110 Tesla, Zenodo (2025), 10.5281/zenodo.17166637.

[39] T. Kameshima, S. Ono, T. Kudo, K. Ozaki, Y. Kirihara, K. Kobayashi, Y. Inubushi, M. Yabashi, T. Horigome, A. Holland, K. Holland, D. Burt, H. Murao, and T. Hatsui, Development of an x-ray pixel detector with multi-port charge-coupled device for x-ray free-electron laser experiments, Rev. Sci. Instrum. **85**, 033110 (2014).

[40] G. Kresse and J. Furthmüller, Efficient iterative schemes for *ab initio* total-energy calculations using a plane-wave basis set, Phys. Rev. B **54**, 11169 (1996).

[41] G. Pizzi *et al.*, Wannier90 as a community code: New features and applications, J. Phys. Condens. Matter **32**, 165902 (2020).

[42] X. He, N. Helbig, M. J. Verstraete, and E. Bousquet, TB2J: A Python package for computing magnetic interaction parameters, Comput. Phys. Commun. **264**, 107938 (2021).

[43] J. Klimeš, D. R. Bowler, and A. Michaelides, van der Waals density functionals applied to solids, Phys. Rev. B **83**, 195131 (2011).

[44] S. L. Dudarev, S. Y. Savrasov, C. J. Humphreys, and a. P. Sutton, Electron-energy-loss spectra and the structural stability of nickel oxide: An LSDA + U study, Phys. Rev. B **57**, 1505 (1998).

[45] S. Kasamatsu, T. Kato, and O. Sugino, First-principles description of van der Waals bonded spin-polarized systems using the vdW-DF + U method: Application to solid oxygen at low pressure, Phys. Rev. B **95**, 235120 (2017).

[46] K. Katsumata, S. Kimura, U. Staub, Y. Narumi, Y. Tanaka, S. Shimomura, T. Nakamura, S. W. Lovesey, T. Ishikawa, and H. Kitamura, The giant magneto-volume effect in solid oxygen, J. Phys. Condens. Matter **17**, L235 (2005).

[47] Y. H. Matsuda, A. Shimizu, A. Ikeda, T. Nomura, T. Yajima, T. Inami, K. Takahashi, and T. C. Kobayashi, High magnetic field x-ray diffraction study of the α phase of solid oxygen: Absence of giant magnetostriction, Phys. Rev. B **100**, 214105 (2019).

[48] See Supplemental Material at http://link.aps.org/supplemental/10.1103/r7br-qnrn for the qualitative analysis of the XRD peak profile and a video for the portable 110 T generation.

[49] Y. Zhao and J. Zhang, Microstrain and grain-size analysis from diffraction peak width and graphical derivation of high-pressure thermomechanics, J. Appl. Crystallogr. **41**, 1095 (2008).

[50] A. C. Murrieta and F. F. Contreras-Torres, Microstructure of polycrystalline solids: A brief review from methods in X-ray line profile analysis, Mater. Today Proc. **48**, 96 (2022).

[51] T. Kakeshita and K. Ullakko, Giant magnetostriction in ferromagnetic shape-memory alloys, MRS Bull. **27**, 105 (2002).

[52] Y. Tokura, Critical features of colossal magnetoresistive manganites, Rep. Prog. Phys. **69**, 797 (2006).

[53] https://youtu.be/J4MT__Raz_k?si=ZDAQnPCsVrjaSUBv

End Matter

Microcryostat—The all-plastic He-flow microcryostat is newly devised for cooling the sample at the coil center down to 10 K, allowing the incident x-ray beam of $\phi \sim 0.3$ mm to hit the sample, whose overview and photo are shown in Figs. 5(a) and 5(b). As shown in the detailed view in Fig. 5(c), the diffracted beam exits from the cryostat, allowing a wide range of scattering angle 2θ from 0° to 45°. The outer diameter of the microcryostat is $\phi 2.6$ mm, which is in the vacuum tube of $\phi 3.6$ mm at the center of the single-turn coil whose inner diameter is $\phi 4$ mm, as schematically depicted in Fig. 5(c). The microcryostat is made of fiber-reinforced plastic and the glue SK-229 (Nitto). The vacuum tube and the microcryostat are held by the 3D printed vacuum chamber made of polylactic acid filament plastic, whose inner surface is coated with the glue SK-229.

Preparation of solid O_2—The film of solid O_2 is condensed at the center of the single-turn coil. As shown in the inset of Fig. 3(c), our microcryostat is further modified for the O_2 sample, where the O_2 gas inlet is directly connected to the cold head of the cryostat. The vacuum tube is also elongated to the beam downstream, with a hole covered with Kapton film ($t = 50$ μm) so that the diffracted x-ray comes out. First, we keep the O_2 gas inlet in a vacuum while we cool the microcryostat. Next, we introduce a limited amount of O_2 gas, which is condensed onto the cold surface of the microcryostat, and then we evacuate the O_2 gas inlet to the vacuum again. We can observe the XRD from the film sample of solid O_2. We estimate the sample temperature from the XRD to be 28 or 35 K. We could not obtain a lower temperature than those, although 10 K is achieved with preprepared solid-state samples. It may be because the additionally installed O_2 gas line works as an additional heat source.

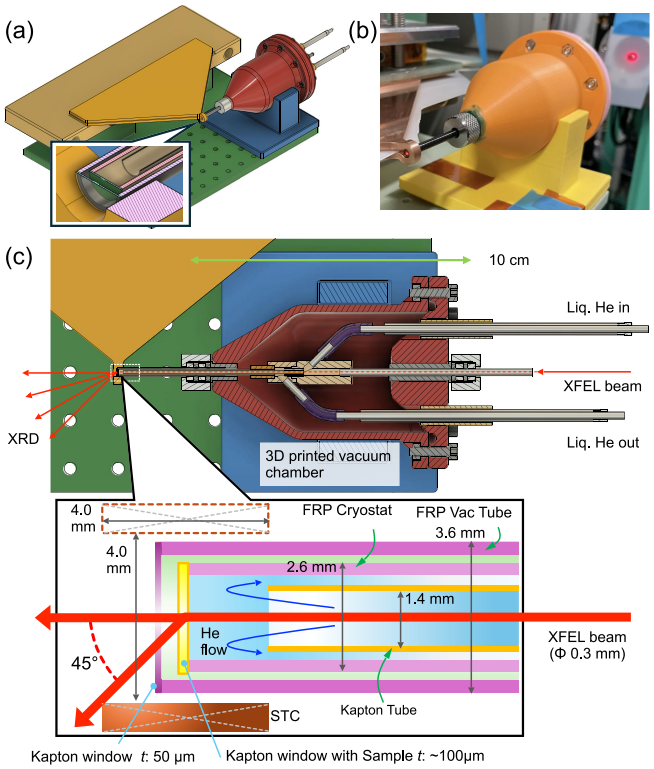

FIG. 5. (a) A schematic of the microcryostat, 3D printed vacuum chamber, and the single-turn coil setup. (b) A photo of the microcryostat, the single-turn coil, and the 3D printed vacuum chamber. (c) Detailed cross-sectional view of the microcryostat, 3D printed vacuum chamber, and the single-turn coil. Fiber-reinforced plastic, FRP.

X-ray detectors—The diffracted beam is detected using two kinds of 2D x-ray detectors. One is a pair of flat panel detectors (FPD) with a distance of 1.0 m from the sample. The other is the multiport charge-coupled device (MPCCD) [39] with a distance of 1.5 m. Single-shot data are recorded at 10 Hz. Three x-ray images are recorded sequentially at $t = -0.1$, 0, and 0.1 ms, where $t = 0$ ms is at the maximum magnetic field. The data of the MPCCD are not presented in the present Letter.

Estimation of exchange interaction using calculations—The first-principles calculation of the exchange constants between the molecular spins of O_2 in solid O_2 was performed using the Vienna *ab initio* simulation package (VASP) [40] in combination with Wannier90 [41] and TB2J [42] packages. First, VASP is used to obtain the electronic structure of β phase oxygen using the vdW-DF-optB86b functional [43] in combination with a Hubbard-U correction [44] of $U_{\mathrm{eff}} = 12$ eV, which resulted in a good description of the α phase of solid oxygen in a previous work [45]. The lattice constants were fixed to those determined experimentally in this Letter, the O—O bond length was fixed to 1.207 Å, and the spin configuration was fixed to the ferromagnetic one. The unit cell in the monoclinic setting was employed with a $5 \times 6 \times 5$ k-point mesh and a plane wave cutoff energy of 1500 eV. Wannier90 was used to obtain Wannier functions and build a tight-binding model with initial projections on the p_x and p_y orbitals of O atoms for π and π^* bands and s orbitals placed at O—O bond centers for the σ bonding band. Only the π and π^* bands contribute to the spin interactions. The resulting tight-binding model was fed into the TB2J code, which uses the Liechtenstein formalism to calculate Heisenberg exchange constants.

Qualitative comparison of the lattice change with a previous XRD report—The significance of the lattice change is consistent with previous XRD studies on the α phase of solid O_2 at 5 T [46] and 28 T [47]. First, a large $\Delta V/V = 1\%$ is reported at 5 T at 7 K [46], later

confirmed as an extrinsic effect by Ref. [47]. Reference [47] further put a constraint that $\Delta d/d < 1 \times 10^{-4}$ at 5 T and $\Delta d/d < 2 \times 10^{-3}$ at 25 T. If we assume the quadratic dependence $\Delta d/d \simeq pB^2$ with typical values of $\Delta d/d = 1\%$ and $B = 100$ T, we obtain $\Delta d/d \simeq 2.5 \times 10^{-5}$ at 5 T, 6.3×10^{-4} at 25 T by an interpolation, which are consistent with the previous XRD study up to 28 T [47], and the present result.

Cooperative softness of the lattice and spin system in β-O_2—We note that the considerable fluctuation of both the spins on the triangular lattice and the arrangement of the molecular axes of β-O_2 may assist the observed significant magnetostriction. The frustrated molecular axis is inferred by the fact that no phase in solid N_2 shows a similar collinear configuration of the molecular axes [6] and also by the thermally induced inverse broadening effect of the XRD peak in β-O_2 [15]. The significant temperature-induced change of the lattice within the β phase of O_2 [Fig. 1(h)] is unique in contrast to the less significant lattice change in α-O_2, where both the spin and lattice are more rigid with the Néel order.

Analysis of the XRD peak profile—The XRD peak widths exhibit a clear dependence on 2θ, and all peaks are broader at 110 T, as shown in Figs. 3(d)–3(f) (see Ref. [48]). Possible origins are a microstrain effect due to anisotropic magnetostriction in random powder, crystal size effect [49,50], and the precursor of the phase transition to θ-O_2 [8] above 120 T; however, they need further evaluation.

Comparison with other giant magnetostriction systems—The present lattice change occurs in the unit cell without a phase transition, which is considered the greatest ever reported to our best knowledge. Larger magnetostrictions are observed in Heusler alloy [51] and manganite systems [52], where the domain's reorientation and the phase transition are the sources of the significant lattice change.

Video of destructive generation of 110 T using a portable 100 T generator PINK-02—See the video of PINK-02 generating 110 T at BL3 in SACLA 13 times successfully in a row (37 sec) in Supplemental Material [48]. The same video is also uploaded to YouTube [53].